Detection of Tornado Damage via Convolutional Neural Networks and Unmanned Aerial System Photogrammetry

Samuel James Carani

Thesis submitted to the faculty of the Virginia Polytechnic Institute and State University in partial fulfillment of the requirements for the degree of

Master of Science
In
Geography

Thomas Pingel, Chair/Advisor
Craig Ramseyer
Yang Shao

September 20th, 2021
Blacksburg, Virginia

Keywords: Photogrammetry, Tornado Damage, UAS, CNNs

Detection of Tornado Damage via Convolutional Neural Networks and Unmanned Aerial System Photogrammetry

Samuel James Carani

Abstract

Disaster damage assessments are a critical component to response and recovery operations. In recent years, the field of remote sensing has seen innovations in automated damage assessments and UAS collection capabilities. However, little work has been done to explore the intersection of automated methods and UAS photogrammetry to detect tornado damage. UAS imagery, combined with Structure from Motion (SfM) output, can directly be used to train models to detect tornado damage. In this research, we develop a CNN that can classify tornado damage in forests using SfM-derived orthophotos and digital surface models. The findings indicate that a CNN approach provides a higher accuracy than random forest classification, and that DSM-based derivatives add predictive value over the use of the orthophoto mosaic alone. This method has the potential to fill a gap in tornado damage assessment, as tornadoes that occur in wooded areas are typically difficult to survey on the ground and in the field; an improved record of tornado damage in these areas will improve our understanding of tornado climatology.

Detection of Tornado Damage via Convolutional Neural Networks and Unmanned Aerial System Photogrammetry

Samuel James Carani

General Audience Abstract

Disaster damage assessments are a critical component to response and recovery operations. In recent years, the field of remote sensing has seen innovations in automated damage assessments and Unmanned Aerial System (UAS) collection capabilities. However, little work has been done to explore the intersection of automated methods and UAS imagery to detect tornado damage. UAS imagery, combined with 3D models, can directly be used to train machine learning models to automatically detect tornado damage. In this research, we develop a machine learning model that can classify tornado damage in forests using UAS imagery and 3D derivatives. The findings indicate that the machine learning model approach provides a higher accuracy than traditional techniques. In addition, the 3D derivatives add value over the use of only the UAS imagery. This method has the potential to fill a gap in tornado damage assessment, as tornadoes that occur in wooded areas are typically difficult to survey on the ground and in the field; an improved record of tornado damage in these areas will improve our understanding of tornado climatology.

Dedication

To everyone who believed in me.

Acknowledgments

I would like to give my deepest appreciation to my family: Maggie, Mom, Dad, Annie, Rose, Molly, Pal, and Bailey. Thank you for always encouraging me to follow my dreams and supporting me through every step of this journey.

Next, I would like to thank everyone who I met throughout my career that helped me get to where I am today. Specifically, Jess, Sarah, Walker, Victor, Dave, and Scott.

I am extremely grateful to Daniel Cross from the Department of Forest Resources and Environmental Conservation for the tornado damage imagery. This whole project was possible because of your work and generosity.

I would also like to thank Mike Sporer and Dr. Wagner for providing advice, facilitating this area of research, and helping bring together this cohort.

I would especially like to thank all the friends I made during my time in the department. The friendship, support, and many laughs were an immeasurable help.

Lastly, I would like to extend my deepest gratitude to my advisor, Dr. Pingel, for the countless hours of mentorship, feedback, and patience. You helped me learn a great deal and develop my skills as a scientist.

Table of Contents

List of Figures

List of Tables

Introduction

Post-tornado response and recovery operations require comprehensive impact assessments to protect lives, property, and accelerate community recovery. However, post-tornado damage assessments in the US, conducted by the National Weather Service (NWS), still heavily rely on community reports and ground verification to generate the assessments (NWS, 2018). Ground based collection methods often lead to uneven coverage, missing data, and slow report turnaround time. These issues are especially prevalent in areas of forest damage where terrain and remoteness can restrict the ability to assess damage. However, damage in forested areas can contain rich information about the tornado size, flow pattern, path, and wind strength. Disaster impact assessments that provide an incomplete picture of the damage can have a significant effect on our understanding of the event and on community recovery.

Unmanned aerial systems (UAS) have the capability of providing timely and detailed information about these rural tornadoes. This thesis examines the potential of UAV-based tornado damage assessment focusing on three main areas. First, a convolutional neural network (CNN) is assessed for its ability to automatically classify tornado damage in a forested area using UAS imagery and Structure-from-Motion (SfM) derived orthophotos and digital surface models (DSM). Second, the efficacy of that model is compared to the more conventional automated technique of random forest classification. Finally, the relative importance of visual (RGB orthophotos) versus spatial (DSM products) products for classification accuracy is assessed.

Research Hypotheses

Due to the advancements in deep learning classification techniques and SfM reconstructions, we expect that a CNN method that incorporates terrain and image derivatives will perform better than an RGB-only CNN. In addition, we expect that a CNN based method will classify tornado damage in undeveloped and forested areas more accurately than the traditional remote sensing technique of random forest classification.

Background

The field of remote sensing has seen profound developments in the aerial and space domains; however, recently terrestrial UAS have proved to be an equally valuable data source. UAS research has spanned a wide variety of scientific disciplines such as ecology (Mulero-Pázmány et al., 2015; Ogden, 2013), geology (Gupta, 2017), forestry (Adão et al., 2017), archaeology (Lin et al., 2011), and civil engineering (Hallermann et al., 2015). UAS offers several benefits over aerial and space systems including rapid collection (Choi et al., 2009; Choi and Lee, 2012), and change detection (Bertin et al., 2020; Nagarajan et al., 2019; Seier et al., 2017). UAS have facilitated a wide range of research in geographic and allied disciplines such as DSM accuracy assessments (Rogers et al., 2020), urban modeling (Choi et al., 2019; Isibue and Pingel, 2020), soil erosion modeling (D'Oleire-Oltmanns et al., 2012), water resource management (Castro et al., 2020; Pingel et al., 2021), vegetation monitoring (Van Iersel et al., 2016; Waite et al., 2019), and traffic analysis (Salvo et al., 2014).

Research on the applications of remote sensing systems for damage assessments spans across a multitude of disasters such as earthquakes (Cooner et al., 2016; Liu and Yamazaki, 2016), floods (e.g. Psomiadis et al., 2019; Rahman and Di, 2017), hail (Bell et al., 2019; Prabhakar et al., 2019; Zhou et al., 2016), fire (Karimi et al., 2019; Samiappan et al., 2019; Singh and Kanga, 2017), hurricanes (Barnes et al., 2007; Radhika et al., 2015; Thomas et al., 2013), and tornadoes (Kingfield and de Beurs, 2017; Wagner et al., 2019; Yuan et al., 2002). Considerable research has been done in the area of multi-spectral analysis particularly (e.g. Huang et al., 2018; Kemker et al., 2018; Mahdianpari et al., 2018), but several studies incorporate data fusion techniques of various sources (UAS, aerial, and space) and sensors to their analysis (e.g. Ghassemian, 2016; Palsson et al., 2015; Skow and Cogil, 2017). A significant portion of the damage assessment work relies on multi-temporal methods. Multi-temporal studies rely on pre- and post-event data to conduct change detection analysis (Ji et al., 2018; Shen et al., 2016; Tuia et al., 2016). A major limitation with multi-temporal methods is that high quality pre-event data is required to provide a strong enough baseline for the post-event data comparison. For example, Tian et al. (2015), found that the pre-event baseline data of Haiti was inadequate for conducting a multi-temporal change-detection analysis for their study.

One common approach to remote sensing damage detection is the use of kernel-based processing on input images. Local neighborhoods are calculated for each pixel and the properties of that neighborhood are then assigned to that pixel. Many of these kernel functions originate from the field of computer vision, where kernels aid in image processing applications such as detecting facial expressions (Xu et al., 2015). Similar kernel-based approaches are found in geomorphology to quantify topography, including calculations of slope, aspect, curvature (Schmidt et al., 2003), openness (Yokoyama et al., 2002), roughness (De Reu et al., 2011; Riley, 1999), and terrain classification (Jasiewicz and Stepinski, 2013; Wood, 1996) among many others. Cooner et al. (2016) utilized several kernel functions in their study including entropy, Laplacian of Gaussian (LoG), and dissimilarity as input training data for their model. Ghaffarian and Kerle (2019) studied texture algorithms including Gabor filters, Local Binary Pattern (LBP), and Histogram of the Oriented Gradients (HOG) to differentiate structural rubble from ephemeral debris. The authors processed UAV mosaics with the different algorithms and found that HOG performed the best at identifying structural debris.

Damage Assessment Using SfM

SfM is an area of photogrammetry (imagery measurement science) that can process 2D imagery collected at overlapping intervals and create 3D models. The overlapping imagery creates a visual parallax that can be used to determine the height and shape of features in the scene. When imagery is collected from an aerial system, GPS coordinates can be tagged in each image. The SfM software can take the geographic information and create an orthorectified (geometrically corrected) photo and 3D model. To produce a high-quality reconstruction; the collection must contain significant imagery overlap (70%+), detailed camera lens and sensor information, and high accuracy GPS coordinates (Haala et al., 2013; Westoby et al., 2012).

A significant area of research has assessed the different methods of UAS imagery collection for the modeling and analysis of earthquake damage. Several articles have focused on case-studies and the construction of 3D meshes and point clouds from UAS-collected images without significant quantification of damage (Dominici et al., 2017; Peng et al., 2018). Yamazaki et al.

(2015) demonstrated a fusion-based approach that combined ground-captured and aerial images to reconstruct 3D mesh representations of buildings damaged in the Tohoku earthquake and tsunami (2011) using a small, commercial-grade UAS, and used a YouTube video to reconstruct damage of the Korgha earthquake (2015) in Nepal. Papakonstantinou et al. (2018), assessed the effect of nadir vs a multi-camera (nadir and oblique) setup on the quality of SfM reconstruction to assess damage. They found that nadir imagery collection alone can miss or underestimate façade damage. Xu et al. (2018) used UASs to image several earthquake sites in Italy and China, and used a supervised, iterative Active Learning-based approach to classify individual points in the SfM point cloud (rather than derivatives such as orthophotos or digital surface models) as debris or not-debris using spectral, textural, and geometric attributes of the points and their K-Nearest Neighbors.

UAS and SfM have been deployed at other environmental disasters such as floods, fires, and hurricanes to aid in damage assessments. Research on UAS-flood applications has primarily focused on studying best practices to deploy systems to respond, identify, and verify flooding. Balta et al. (2015) presented a case study on the use of UAS to assess flooding in the Balkans and investigate possible landmines (war remnants). Murphy et al. (2016), flew 21 missions for two different floods in Fort Bend County, Texas for emergency management purposes and damage assessments. The authors detail the timelines and processes to deliver damage assessment products to stakeholders and conclude that current UAS strategies and photogrammetry software may not satisfy ROI depending on stakeholder needs because of the complexity of the software and the licensing cost. Salmoral et al. (2020) conducted a review of different UAS collection strategies for flood events and developed a Deployment Analysis Matrix to aid operators in focusing and targeting UAS collection for flood events.

Researchers have also deployed UAS to collect imagery for damage assessments of wildfires. Samiappan et al. (2019) implemented UAS to collect multi-spectral imagery for post-fire damage analysis. The imagery allowed the authors to calculate NDVI and compare the change in multi-spectral reflectance to assess the extent of the damage and the vegetation recovery. Carvajal-Ramírez et al. (2019), compared pre- and post-event fire multispectral imagery collected by a

UAS-SfM in a Mediterranean forest and found that NDVI difference performed the best at characterizing fire damage among several different fire indices.

Hurricanes damage assessments have seen a similar impact of UAS. Mohammadi et al. (2019), classified damage with 3D point clouds (derived from UAS-SfM) collected from post-event Hurricane Harvey. They used CNN to semantically segment their data into different classes of damage, undamaged, and debris. Their model was trained on one site, Salt Lake, and tested on a second site, Port Aransas. The authors found that their models performed well at classifying neutral/terrain features and in transferability between sites; however, precision did suffer when classifying objects that shared similar geometry and color. Brodie et al. (2019), examined the ability of UAS collections to quantitatively assess Hurricane Irma coastal impact. They collected data at three different Florida sites and compared SfM (Photoscan Professional) point cloud to aerial lidar collections. The authors found that the UAS-SfM point clouds performance was similar to the aerial lidar collections and would be a valuable data source for quantifying post-event impacts.

Photogrammetrically derived DSMs have similarly been used in a variety of contexts for damage assessment including flooding (Anders et al., 2020; Bodoque et al., 2016), coastal storm damage (Udo et al., 2018), earthquakes (Menderes et al., 2015; Tian et al., 2015; Yamazaki et al., 2015), wildfires (de Roos et al., 2018; Samiappan et al., 2019), and storm damage (Honkavaara et al., 2013). Anders et al. (2020) studied the effects of flight altitude and orientation on the accuracy of the resultant UAS-SfM-DSM and the ability to conduct a flood damage assessment. They found that different flight altitudes did not significantly change DSM vertical accuracy nor the horizontal accuracy of the SfM orthophoto. The different collection orientations resulted in a different elevation value of 10 cm to 20 cm. However, the authors conclude that they could successfully conduct manual damage assessments with the DSM. De Roos et al. (2018), used a UAS-SfM-DSM method to build a hydrological model to assess how fire damaged Sphagnum peatlands would recover.

Several studies have implemented pre- and post-event DSM difference (dDSM) to calculate surface change to identify damage. Honkavaara et al. (2013) created a dDSM from aerial lidar

and high-altitude photogrammetry. The dDSM was then used to analyze forest damage caused by a Finland winter storm in 2011. The authors found they could accurately identify fallen trees via dDSM. Udo et al. (2018), used ERDAS IMAGINE to create a dDSM of the 2011 Sendai Coast Tohoku Earthquake Tsunami damage. The authors were able to visually verify and statistically detect tsunami damage via the dDSM using frequency distribution analysis. The authors note that due to noise, damage to low ground objects was harder to assess. Menderes et al. (2015), generated normalized DSMs (nDSM = DSM - DTM) from pre- and post-event stereo aerial photos. The authors used thresholds to automate damage detection. With their method, the authors were able to achieve an overall accuracy of 96.54% and 90.74% and a kappa of 82.50% and 56.93% for their two test regions.

Deep Learning Approaches to Damage Classification

Convolutional Neural Networks (CNNs) have recently been used in a variety of remote sensing classification applications, including damage assessment. CNNs are a type of deep learning algorithm that is designed to mimic the way an animal's visual cortex neurons interpret images (visual field). The input image is passed to a convolution layer, which applies a kernel function to each channel of the imagery. The results of each channel kernel output are summed into a single channel output called a convoluted feature. The output is then passed to a pooling layer which focuses on extracting significant features to reduce dimensionality. The pooling layer applies either a max pooling (maximum pixel kernel) or an average pooling (mean pixel kernel). The output is then passed to the fully-connected layer which attempts to find non-linear combinations in the output. The output is converted into vectors that are passed to a feed-forward neural network (multi-layer perceptron). After several iterations (epochs), the feed-forward neural network identifies features and passes the output to a classifier. After this phase is complete, the output is a model that can be used to classify data.

One significant application of CNN-based methods is in the problem of mono-temporal classification, in which no equivalent pre-event imagery exists to which post-event damage imagery can be compared. Heydari and Mountrakis (2019), performed a meta-analysis of mono-temporal classification papers that implemented deep neural networks in their work. The authors

found that CNNs were the most used type of model for mono-temporal classification and that they generally performed better than other deep learning methods. Many of the CNN damage detection implementations utilize semantic segmentation to classify objects and damage into classes. For example, segmenting houses and classifying each house into damaged or non-damage.

Vetrivel et al. (2016) developed a method that integrates CNN feature extraction (object segmentation) with a Passive-Aggressive online classification to detect structural damage in imagery delivered on-the-fly to the system. Their method allows damage assessments to be computed faster and with lower memory resources. The authors found their damage assessment model performed better than conventional handcrafted features (gray level co-occurrence matrix and Gabor wavelets). As mentioned previously, Mohammadi et al. (2019) implemented a semantic segmentation method and CNN to categorize damage and undamaged features. Ma et al. (2020) does not use a segmentation method but uses block groups as a segmentation proxy. The authors create a CNN that can determine the degree of damage to groups of buildings damaged by an earthquake. The authors method does not perform segmentation because they are using block boundaries (GIS) to segment the imagery. This allows the model to extract damage information for groups of buildings. The authors found that their method was able to detect damage, however, authors note the model had difficulties identifying collapsed buildings and differentiating bare ground. Not all CNN damage assessment papers implement a segmentation method. Fujita et al. (2017) use a CNN to detect "washed away" tsunami damage. Their model was trained on pre- and post-tsunami imagery tiles. Their method achieved a total accuracy (percentage of correct classifications for a given sample) of 94-96%.

Tornado Damage Assessment

In the United States, current tornado damage assessments are conducted by the US National Weather Service (NWS). The NWS outlines their operations and methods in an NWS directive (NWS, 2018). When a tornado occurs, the NWS utilizes weather radar, storm spotter reports, and news/social media coverage to get an estimate of the tornado path. After the event passes, NWS personnel go to individual reports of damage and catalog the incident in the NWS Damage

Assessment Toolkit app. The data is then uploaded to NWS networks and made available to the public via the NWS Storm Damage Viewer online portal. This process is labor-intensive, making the turnaround time of post-event damage assessments slow. Wooded areas are often under assessed areas of damage because the affected areas can be difficult to reach. This is because forested areas can be restricted by access, hazardous terrain, and remoteness. After a disaster, assessments prioritize property damage and loss of life over environmental damage. In events where damage assessment resources are limited, damage to forested areas may not be assessed at all.

Remote sensing-based approaches to quantifying or classifying tornado damage often use multispectral and multi-temporal approaches. Vegetation indices such as NDVI are often used to investigate vegetative damage and recovery (Kingfield and de Beurs, 2017; Yuan et al., 2002). Kingfield and de Beurs (2017) utilize multi-spectral imagery to investigate how the spectral signature of tornado damage changes over different land-cover types. The authors utilize a mono-temporal method (post-event damage analysis) to measure spectral change. They found that tornado-damaged areas exhibited a higher median reflectance in the visible and shortwave infrared, and a lower median reflectance in the NIR range. Damaged areas experienced a higher median Tasseled Cap brightness, lower Tasseled Cap greenness and wetness, and lower NDVI.

Recent work has used traditional remote sensing classification techniques and computer vision algorithms to detect tornado damage. Cannon et al. (2016) created a supervised classification algorithm (maximum likelihood classification) in ArcMap, to classify tornado damage severity on aerial photographs in order to determine the characteristics of damage in mountainous terrain. The authors found a significant relationship between the classification's severity with ground-truth assessments with an accuracy of 88.5% to 93.4%. They also found that damage severity decreased as the tornado path ascended ridges. Womble et al. (2018), provide a comprehensive review of various remote sensing systems and the associated challenges of collecting tornado damage information at different scales, and note that UAS-based assessment has several advantages over satellite-based collection, including being less sensitive to cloud cover and atmospheric conditions. Additionally, the large number of images collected by UAS allow for the generation of detailed 3D models that can aid in manual damage assessments. However,

Federal Aviation Administration regulations currently restrict UAS operations to only line-of-sight which impedes user's ability to collect large damage areas; beyond line-of-sight (BLOS) operations are currently under active review. Wagner et al. (2019) found that UAS outfitted with multispectral cameras add significant value by improving tornado path detection over simple RGB imagery.

Published research on the applications of UAS photogrammetry and computer vision to detect tornado damage is limited. Wagner et al. (2020) presented ongoing research on using UAS-SfM orthophotos and a segmentation-based deep neural networks (DNN) to detect damage to roofs and residential homes. Their preliminary results look visually impressive and gives high confidence in the ability to classify tornado damage with DNN techniques. Follow up work by Chen et al. (2021) quantitatively assessed several deep learning model schemas for tornado damage detection and found that binary classification (damage / no damage) had higher accuracy rates than multi-classification systems (e.g., major, minor, and no damage). Among several different deep learning model backbones, they found that DenseNet-161 with a binary schema, had the highest overall accuracy at 84.8%. ResNeXt-101 performed the best among the multi-class schema at 81.5%.

Methods

Following work by Wagner et al. (2020) and Chen et al. (2021), a CNN classifier is developed and tested to distinguish between damaged and undamaged forest. This is done by constructing an orthomosaic with SfM on a collection of RGB images taken by UAS over an EF-3 tornado track through a forested area in western rural Virginia.

Study Area

UAS data for this research was from the April 19th, 2019 Franklin County Virginia tornado (NWS, 2019) centered on an area approximately 8 km SSE of Rocky Mount, VA in the southwest part of the state (Figure 1). The tornado formed at 10:25 am just north of Oak Level and travelled for approximately 13.2 km where it dissipated just east of Henry Fork at around

10:35 am. The tornado reached a peak intensity of EF-3 (159 mph) and an estimated maximum width of 250 m near Windy Ridge Road. According to NWS surveys (2019); the tornado severely damaged three structures, destroyed ten outbuildings, and caused 2 injuries (no deaths).

Data Sources

Daniel Cross (Virginia Tech: Department of Forest Resources and Environmental Conservation) collected imagery of the tornado damage on April 29th, 2019 with an eBee fixed wing UAS. Cross flew a 3.6 km section of the tornado track between US Highway 220 and Sontag Road near the Franklin County Parks and Recreation Center. The UAS flew at an altitude of 400 feet (122 m) above ground level (AGL) and collected 601 images with the onboard senseFly S.O.D.A. camera (20 MP; 3,648 x 5,472 pixels; f/2.8; ISO-125; 11mm focal length; 2.97 max aperture) with a calculated overlap of 60% and a sidelap of 75%. A lidar derived DTM (1-meter resolution) from a 2018 VGIN aerial survey was used for the creation of the Canopy Height Model layer.

The truth dataset, used in training and cross-validation of the model, was created from manual imagery analysis of the RGB orthophoto. As seen in Figure 2d, polygons were drawn over forested areas that appeared to be damaged. Initially, individual tree stems visibly disturbed by the tornado were flagged as linear features, with a kernel density aggregation used to quantify damage. However, among independent human classifiers there was not always strong agreement where damage was heavy. As a result, simple polygons were used to classify damage (presence / absence). Several passes and spot checks (at different zoom levels) were done to verify the classification. Although a finer damage classification may be possible, the result of using this method is that the deep learning model is effectively trained to detect this method of damage marking.

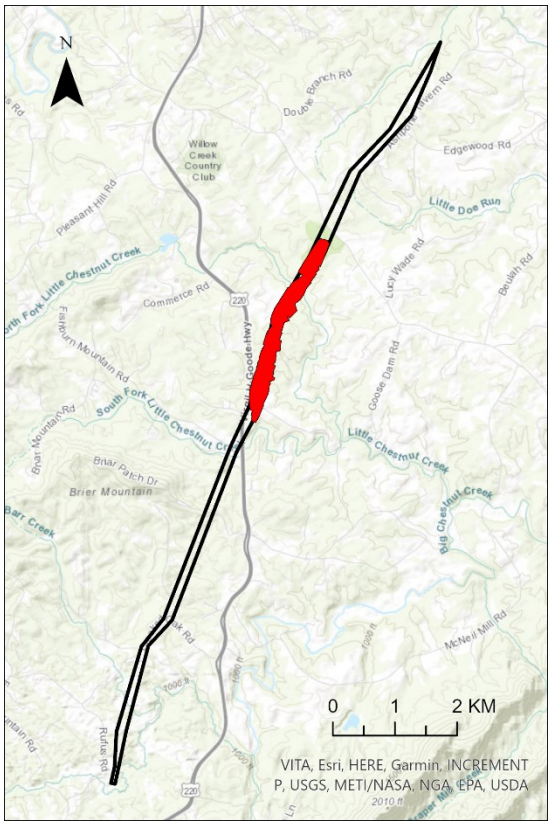

Figure 1. NWS path of the Franklin County Tornado (black) and the study area (red).

Materials

A Dell Precision 5820 workstation running Windows 10 Enterprise (20H2) was used for computation. The computer is equipped with an Intel Core i9-9980XE CPU (3.00GHz, 18 Cores, and 36 Logical Processors), 128GB of RAM (non-ECC), and a Nvidia GeForce GTX 1080 with 8GB of Video RAM. Software used for data processing included Esri ArcGIS Pro (for deep learning) and Pix4Dmapper (photogrammetric processing).

Structure from Motion Processing and Generation of Derivatives

Imagery was processed in Pix4Dmapper to create the orthophoto and point cloud using settings detailed in Appendix A. The SfM software matched 557 of 601 images with a nominal ground

sampling distance (GSD) of 2.79 cm. In order to reduce processing time, the orthophoto and DSM were generated at 10 cm resolution. A lower resolution layer could have been generated; however, 10 cm was used because it preserves the detail of the damage; a coarser resolution image started to lose detail that seemed likely to be helpful in classifying damage. The point cloud was generated using the "optimal" setting in Pix4D, which created a dense point cloud of 379.9 million points (573 points per square meter).

Due to the complexity of the forest canopy, a large number of "voids" remained in the Pix4D output DSM. To repair these, the raw point cloud was cleaned of outliers using CloudCompare point cloud processing software and then imported into ArcGIS Pro (v. 2.7) for DSM generation. The ArcGIS Pro *void fill* geoprocessing tool was used (max void width 4) to fill voids in the DSM. The small radius was chosen to reduce the appearance of artifacts in the DSM where voids were too large to interpolate reliably. As a result, some limited areas within the DSM remained unfilled; these were flagged during model preparation and excluded from analysis. The resulting orthophoto and DSM are shown in Figure 2.

In addition to the RGB channels, several metrics were calculated and added to the raster (Tables 1 and 2). Entropy (measure of randomness) and LoG (second-order spatial derivative kernel filter) are the image derivatives calculated from the RGB orthophoto. In addition to elevation (the DSM itself), several DSM derivatives were calculated including the Canopy Height Model (the difference of the Virginia VGIN lidar DEM and DSM), multi-directional hillshade, openness (portion of the sky visible, including negative relief), profile and tangential curvature (second derivative of the surface), standard deviation of slope, and Vector Ruggedness Measure (a neighborhood metric of surface "roughness") introduced by Sappington et al. (2007). These were selected based on their use in previous studies to characterize different aspects of the land surface (Amatulli et al. 2018). The image derivatives (entropy and LoG) were generated in Python with scikit-image and the DSM derivatives were created in ArcGIS Pro (Canopy Height Model, multi-directional hillshade, standard deviation of slope, profile and tangential curvature) and SAGA (openness and Vector Ruggedness Measure).

To prepare data layers for inclusion into the CNN model, each derivative was stretched and scaled to an unsigned 8-bit integer. This was done because the arcgis.learn module requires this specific data type. Layers were scaled such that the 5th and 95th percentile were set to the minimum and maximum values in the range as a way to enhance contrast and reduce the impact of outliers in the data. Any pixels that remained as voids in the DSM derivatives (except for CHM), due to the small interpolation kernel, were flagged as null and excluded from analysis. All layers were then grouped together into a 14-band (including the RGB alpha channel) combined raster stack. This final multi-band image was ready for processing with the arcgis.learn workflow.

Several layers required a kernel size (or neighborhood) parameter for their computation. Three circular kernel radii were tested to determine the effect of kernel size on model performance: 5px (0.5m), 25px (2.5m), and 50px (5m). These sizes were chosen to sample several plausible scales at which tornado damage would be apparent.

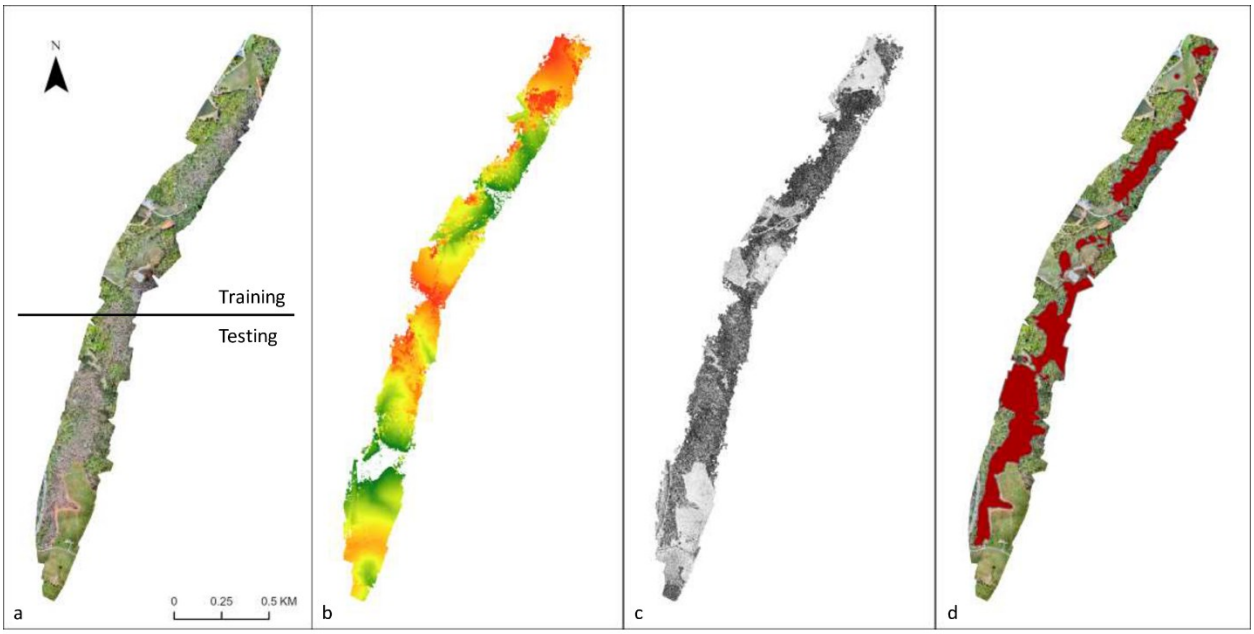

Figure 2. Orthomosaic (a), DSM (b), hillshade (c), and damage polygons (d) of tornado study area.

CNN Model Development

The study area orthophoto was split (approximately 50/50) into a northern (training) and southern (testing) subset. Each of the two sections had similar damage and no damage profiles. Separating the orthophoto into a training and testing dataset allowed for independent testing to verify the model performance. For ArcGIS to initiate training, the training section of the multi-band raster was chipped into 512x512 pixel "chips" (imagery tiles) with 256x256 pixel overlap. To increase training data, each chip was rotated 3 times (0, 90, 180, and 270 degrees) with ArcGIS Pro to create a more diverse training set, as is commonly done (ESRI, 2021). Imagery rotation also helps reduce the possibility of directional bias in the model. In total 6,328 chips were created for training.

Training of the model was completed in ArcGIS Pro with the deep learning model creation toolbox. An iterative approach was taken to optimizing the models hyperparameters. Each model is trained on the training dataset with a given set of hyperparameters (learning rate and epoch). The resultant model's classification performance statistics are calculated by cross-validating against the testing dataset. These results are then compared to other models with different hyperparameters (same testing and training regions). An optimal learning rate and epoch is chosen by selecting the model with the highest kappa value (calculated on the training dataset cross validation). This model and the corresponding hyperparameters are used for the rest of the analysis.

Evaluation of the model performance was conducted in ArcGIS Pro / ArcPy, and custom Python scripts. ArcGIS Pro was used to classify imagery and render the model output. Custom Python scripts were used to statistically analyze the classification performance with skimage using F1 score (harmonic mean of precision and recall), Cohen's Kappa (level of the classification agreement with the occurrence of chance removed), precision (true positives divided by the sum of all positives), recall (true positives divided by the sum of true positives and false positives), as well as overall accuracy (correctly classified pixels divided by total pixels). Kappa will primarily be used in this analysis to measure the classification performance of the model on the testing dataset because the statistic removes the model's probability of classification agreement by

chance. In addition, an orthophoto-only model (with no image or DSM derivatives) and a traditional random forest model are used as controls to compare the results to. Random forest is an ensemble type machine learning technique (commonly used in remote sensing) that creates decision trees to classify data. The random forest model is built with scikit-learn on the entire multi-band raster stack.

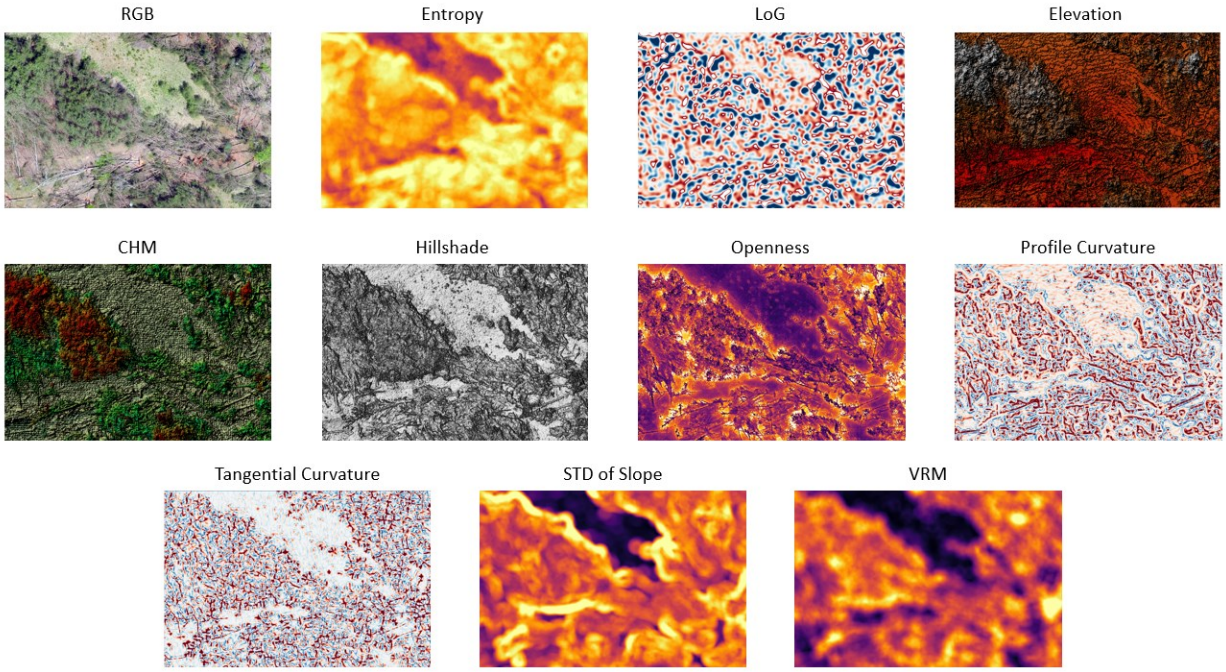

Table 1. Visual representation of model input layers.

Source	Layer	Description
Orthophoto	Entropy	A measure of the average level of order/disorder in a neighborhood within a grayscale image. Calculated using scikit-image.
	Laplacian of Gaussian (LoG)	Second-order spatial derivative kernel filter to highlight edges. The image is first convolved by a gaussian filter (low pass filter) and then passed to a Laplacian filter, equivalent to general curvature. Calculated using scikit-image.
DSM	Canopy Height Model (CHM)	The difference between a Digital Terrain Model (ground surface) and a DSM, which may include vegetation and buildings. The resultant raster is a "flattened" surface model and represents surface features with major elevation changes removed. Calculated in ArcGIS Pro using a secondary lidar-derived DTM.
	Multi-directional Hillshade	Illumination of the DSM is modeled from multiple angles creating a 3D visualization of the surface. Calculated in ArcGIS Pro.
	Openness	A neighborhood calculation of the sky visibility (including negative relief) from a central pixel. Calculated in SAGA.
	Profile Curvature	Second derivative of the surface in the vertical plane. Profile curvature helps illustrate the rate of change of surface features parallel to slope. Negative values represent convex slopes while positive values represent concave slopes. Calculated using a neighborhood (*Surface Parameters* tool) using ArcGIS Pro.
	Tangential Curvature	Second derivative of the surface perpendicular to the slope gradient. Tangential curvature measures the rate of change perpendicular to slope. Negative values indicate convex slope in the perpendicular plane and positive values indicate concavity. It is similar to contour curvature which describes where landforms bend "out" or "in". Calculated using a neighborhood (*Surface Parameters* tool) using ArcGIS Pro.
	Standard Deviation of Slope	The variation of slope values in a given neighborhood of a central pixel. Low values indicate a more uniform surface, positive values indicate a larger variation in slope values. Calculated in ArcGIS Pro with the *Focal Statistics* tool.
	Vector Ruggedness Measure (VRM)	A neighborhood metric of surface roughness based on a vector decomposition of the surface within a specified neighborhood. Calculated in SAGA.

Table 2. Image and DSM Derivatives (in order of multi-band stack, except DSM).

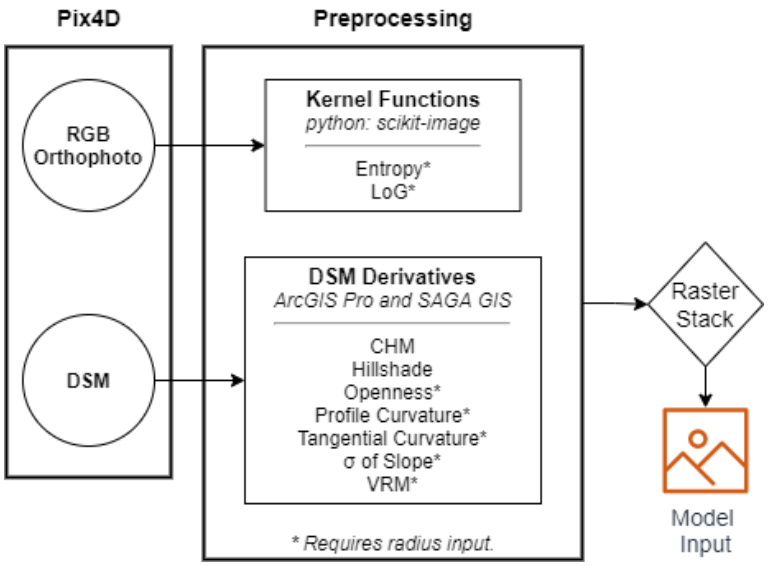

Figure 3. Input layers for the CNN model.

The chipped data, as seen in Figure 3 and 4, are then passed to the arcgis.learn training functions. The CNN used a UNET pixel classifier with the RESNET34 (34 layer residual neural network) backbone. To train the model, the training data, learning rate (the step size of each iteration), and epochs (number of model iterations) were passed to initiate training. After the training is complete, a pytorch model was exported. The model was then used to classify the test imagery and was compared with the truth dataset to assess classification performance.

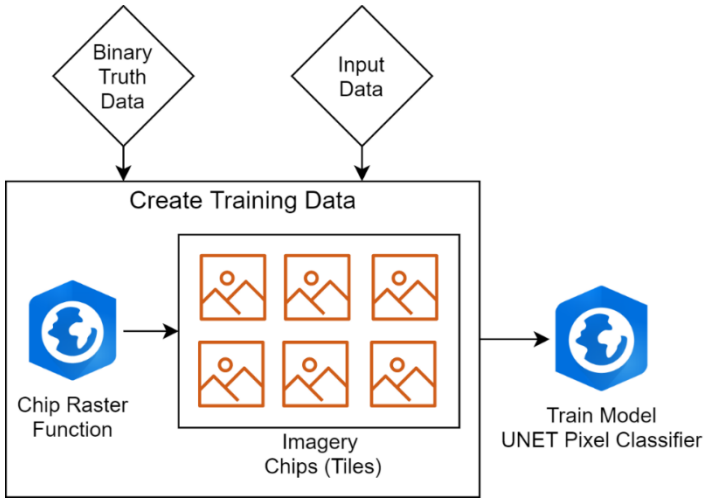

Figure 4. ArcGIS Pro model creation workflow.

Results

Kernel Size and Learning Rate

For each of the three kernel radii (.5, 2.5, 5.0 m), a CNN model was created and assessed. Each model was run with a learning rate of $1x10^{-5}$ at 20 epochs because preliminary testing indicated that the optimized parameters would be close to these values. Differences in accuracy rates for the different kernel sizes were small, with 2.5 m showing the largest kappa accuracy score (71.3%) followed by 5.0 m (kappa = 70.0%) and 0.5 m (kappa = 68.9%). Due to its higher kappa value, subsequent model testing only utilized the 2.5 m radius derivatives. The primary model hyperparameters were then optimized through iterative testing, by adjusting the learning rate between $1x10^{-6}$ - $1x10^{-4}$ and the epochs between 10 and 30. Approximately 20 models were created in this iterative testing to find the optimal learning rate of $2x10^{-5}$ at 25 epochs. The model achieved a kappa of 78.0% and an F1 score of 87.3% on the full multi-band dataset.

Model Performance

The full dataset model achieved a kappa score of 78.0% and an F1 score of 87.3% (Figure 6 and Table 3). In order to assess the contributions of RGB alone, a second model was run using only the orthophoto as input; this model was slightly worse than the full model, with a kappa of 73.5% (F1 = 85.8%). Visually (Figure 5), the output of the two models looks similar and both classify most of the visually identifiable damage. The full model that includes the DSM derivatives tends to capture the damage areas with more precision (85.7% vs. 76.5%) and fewer false positives, while the RGB-only model tends to overclassify damage in some areas. To compare to non-Deep Learning methods, a simple random forest model was built using scikit-learn (Pedregosa et al., 2011). The random forest model (50/50 testing-training ratio) achieved a kappa of 60.1% (F1 = 76.9%), which is lower than the CNN results. There are likely several factors contributing to this difference, however, a possible hypothesis is that the CNN feature matching enables the model to assess spatial differences and identify damage features better. The random forest model is a pixel-based classifier that evaluates the damage in an isolated pixel-by-pixel approach.

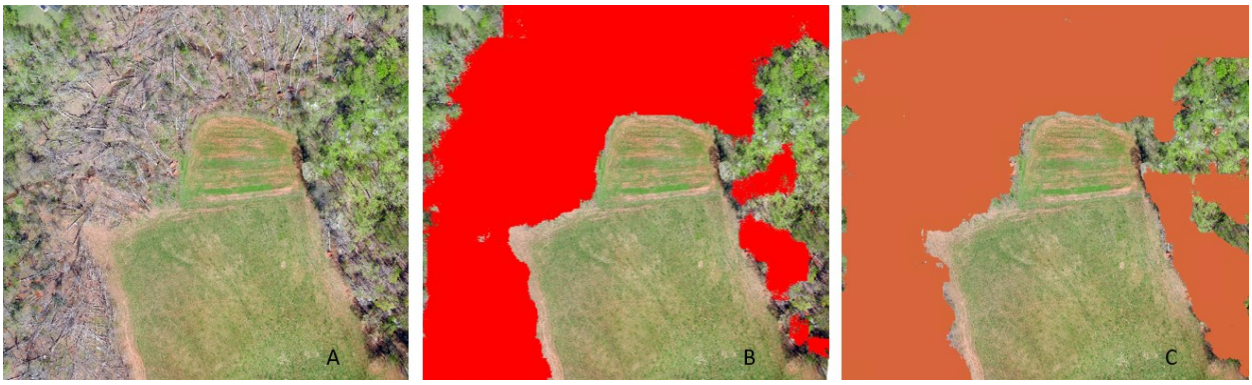

Figure 5. Orthomosaic of a portion of the study area (A), model output for all layers as inputs (B), and RGB-only model (C).

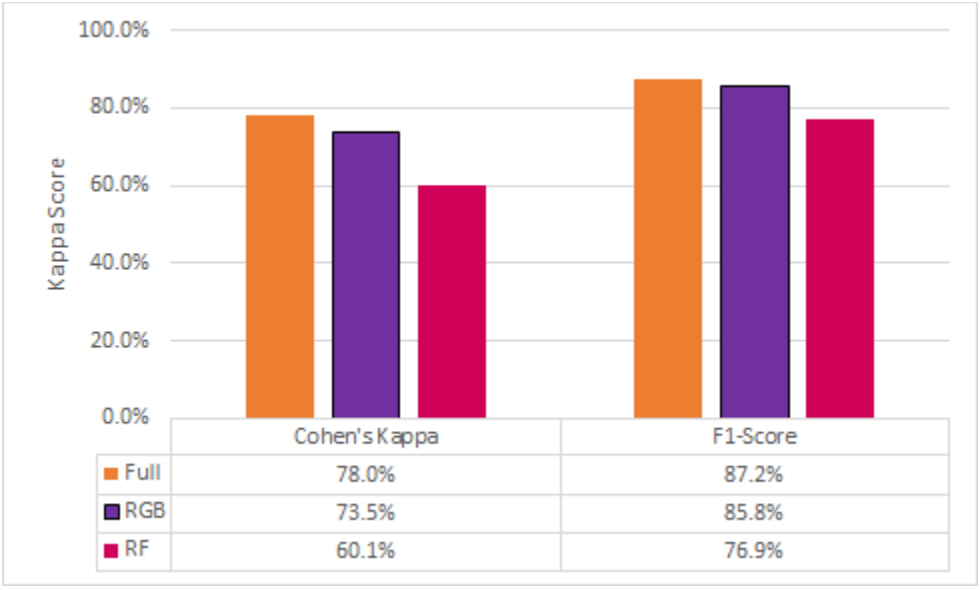

Figure 6. Performance of three main models (%): the full multi-band model, the orthophoto only model, and a multi-band random forest model.

In order to understand the ability of each image and DSM derivative contribution to the overall CNN, separate models were generated (with the same hyperparameters as the full model; learning rate of $2x10^{-5}$ at 25 epochs). These hyperparameters were not individually tuned for each model and may be contributing to under- and over-training of the models. However, this analysis was performed to measure the ability of each layer to classify damage and estimate the

contribution to the overall model. Figure 7 and Table 3 shows a breakdown of each derivatives kappa score in comparison to the RGB only model. The full model had a marginally higher kappa value (78.0%) than the RGB only model (73.5%); the derivatives add 4.5% kappa to the overall model performance. However, the breakdown of each layer indicates that there are significant differences in the ability of certain layers to classify damage than others. The lowest performing derivatives were the image-based entropy and LoG bands. In comparison, the DSM derivatives were much better at classifying damage on their own. Among the DSM derivatives, Vector Ruggedness Measure (VRM) performed the highest at 68.4% kappa. Tangential curvature, openness, hillshade, CHM, and the DSM performed around the same level of kappa, 58.5% to 63.5%. The lower performing derivatives were standard deviation (STD) of slope and profile curvature at 49.2% and 38.1% kappa, respectively. The Canopy Height Model, which used a lidar layer to subtract out ground elevation from the DSM, performed better than the DSM itself, likely because it allows vegetation height to feature more prominently. Other than the VRM, the easily-calculated and common hillshade (or shaded relief) layer performed second-best.

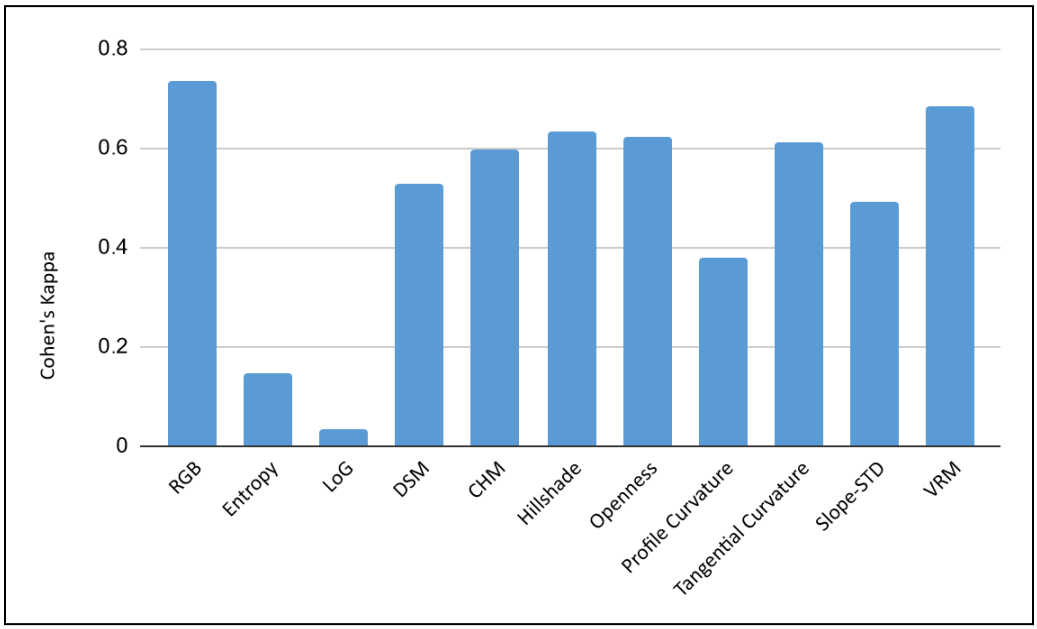

Figure 7. Single-layer model performance for all input layers.

Model	Accuracy	Kappa	F1	Recall	Precision
Full	89.3	78.0	87.2	88.9	85.7
RGB	86.6	73.5	85.8	97.7	76.4
Entropy	63.6	14.8	26.5	15.9	79.7
LoG	59.8	3.4	7.2	3.8	75.6
DSM	80.1	58.5	75.2	73.2	77.3
CHM	80.8	59.7	75.3	70.9	80.2
Hillshade	82.1	63.5	79.1	82.3	76.2
Openness	81.2	62.2	79.0	85.4	73.5
Profile Curvature	72.6	38.1	52.9	37.2	91.4
Tangential Curvature	81.1	61.0	77.0	76.6	77.4
Slope-STD	76.6	49.2	65.7	54.3	83.3
VRM	84.8	68.4	81.2	79.9	82.6
Random Forest	80.5	60.1	76.9	78.6	75.3

Table 3. Computed statistics (%) for each model, and the derivatives breakdown.

Discussion

Although it was expected that kernel radius size (.5, 2.5, 5.0 m) to generate the various derivatives (both RGB and DSM-derived) would have a significant impact on performance, this was not the case, with kappa values nearly identical. A possible explanation for this effect is that the derivatives, in general, only added a 4.5% of kappa over the RGB-only model. Any significant changes in the effect of the derivative bands would be relatively small in comparison to the already significant effects of the RGB bands.

The full model including RGB, DSM and various derivatives performed well with a kappa score of 78.0%. However, the RGB input by itself was also quite predictive (kappa = 73.5%). Several factors might be contributing to these results. The truth damage data was created by creating polygons from the RGB layer. The derivatives might be revealing damage that might not be seen

on the RGB, or conversely, damage that was classified on the RGB was not apparent in the derivatives. This effect would propagate to the model and cause some of the difference we observed. Another possible explanation is that the radius size might need to be specifically adjusted for each derivative. We selected one radius size for all of the derivatives, however, this might lead to some derivatives under-performing because that specific radius might not be appropriate for that particular layer. Individually tuning the radius of each derivative might improve the overall model performance.

The comparison of kappa for each derivative layer indicated that there are somewhat significant differences between each layer of the model. While the test is not perfect, it appears to show that the DSM derivatives are promising additions to the overall model performance, especially the VRM layer. The kappa scores for the image-based derivatives are significantly lower than for the DSM based derivatives. The reason for these results is unclear, but surprising given that Cooner at al. (2016) found both entropy and LoG to be useful layers in damage classification. Earlier, when the three radii were tested, all radius derived bands were all set to the same value. This was done to reduce the complexity of the experiment. It is possible that the 2.5m radius was a better fit for the DSM derivatives than the image derivatives. Equally possible is that the DSM derivatives are a significant addition to the model and outperform the image derivatives. However, a more in-depth analysis of individual band performance is needed to determine the exact relationship.

To combine all the layers together, each derivative needed to be scaled to an unsigned 8-bit integer format. Each derivative was clipped to 5% and 95% and then stretched to 0-255. This was done to satisfy the deep learning input requirements and to normalize the layers. This clipping and stretching might have had an impact on the overall model performance. Further research would need to be done to analyze the effect of this stretch and compare it to different methods, such as a standard deviation clip.

Wagner et al. (2020) and Chen et al. (2021) showed that CNNs and deep learning algorithms can be trained to classify UAS-derived residential damage from tornadoes, and reported accuracy rates of 81-86%. Total accuracy (rather than kappa) was 89.3% for the full model, 86.6% for the

RGB layer, indicating better or comparable performance, despite the difference in application (forest vs residential damage). The Wagner et al. (2020) and Chen et al. (2021) workflow incorporates an extraction layer to identify homes and determine whether the home is damaged or undamaged and to what degree. In contrast, this study used a simple binary (damaged/undamaged) pixel-classifier and does not contain any extraction layers or degree of damage classifications. Furthermore, our study focuses on the identification of tornado damage with mono-temporal UAS datasets as opposed to multi-temporal (change detection) studies. Mono-temporal data is the primary source of tornado damage imagery and the development of these techniques are an important area of study in the damage detection field.

Menderes et al. (2015), found their nDSM change classification method was able to achieve an overall accuracy of 96.54% and 90.74% and a kappa of 82.50% and 56.93% for their two earthquake damage regions. Their results, in combination with the DSM derivative results from this research, indicates that DSM products can add value to damage classification algorithms over orthophoto-only classification. The extent of this effect needs further research. Fujita et al. (2017) CNN tsunami damage model achieved an overall accuracy of 94-96%. The Chen et al. (2021) UAS tornado damage model, when built with different backbones, achieved 84.8% with DenseNet-161 (binary schema) and 81.5% with ResNeXt-101 (multi-class schema). In this research, the full-model from this study achieved an overall accuracy of 89.3%. The three studies achieved results in the same range, indicating that CNNs are effective at classifying damage. Further research is needed to determine the robustness of CNN based damage models and the sensitivity to different damage sites.

Limitations

Pix4D processing reconstructed the 3D point cloud, DSM, and orthophotos from the input georeferenced images collected by drone. Voids left in the DSM were ultimately caused by an insufficient number of images in some locations; complex areas such as rugged terrain or forest canopies often require higher image overlap than simpler scenes (Fraser and Congalton, 2018; Haala et al., 2013). One would expect that if the resultant DSM had better coverage and fewer holes, the model would perform marginally better.

Performance tuning was performed serially, radii and then hyperparameters. The underlying output is based on the initial radius test. To reduce computational expense, the better performing radius was chosen for the rest of the tests. It is unknown what the performance would be of the other radii. The performance of this model with other types of imagery like satellite, aerial, and other UAS platforms was also not tested in this thesis. Given the difference between our input resolution (10 cm) and coarser satellite-based imagery, we expect that models developed for UAV-based products may work differently than they would on satellite-derived products. Since this study only used 10 cm data, the effect of input resolution on model classification performance is not known and would require further testing.

Future Research

An area of research inspired by Chen et al. (2021) is to compare different model backbones on the overall classification performance. There are a variety of CNN backbones and methods for binary pixel classifiers that could potentially alter the model's performance. Another area of further research is to examine more image and DSM derivatives and evaluate each derivatives ability to identify damage and no damage pixels. This thesis focused only on a single tornado; a limitation caused by a notably quiet period in tornado occurrence in the region. Future research should include more events in a variety of geographic regions. Incorporating more data could improve the classification performance and the robustness of the model. In addition, more events would allow for further analysis of the model's ability to classify damage and no damage in different environments. Finally, an assessment of common features or environments that cause the model to misclassify the imagery will be conducted in future research.

Conclusion

Post-disaster damage assessments are a critical component to response and recovery operations. UAS platforms prove to be useful tools for imagery collection and for post-event surveys. A CNN model was built to identify tornado damage from UAS orthophoto, image derivatives, and DSM derivatives. Our results indicated that (a) a Deep Learning approach performed better than

other machine learning (i.e., Random Forest) approaches, (b) that the RGB orthophoto alone performed nearly as well as the full 14-layer model, (c) that among the spatial DSM derivatives, the Vector Ruggedness Measure and the easily calculated multidirectional hillshade performed the best.

References

Adão, T., Hruška, J., Pádua, L., Bessa, J., Peres, E., Morais, R., Sousa, J., 2017. Hyperspectral Imaging: A Review on UAV-Based Sensors, Data Processing and Applications for Agriculture and Forestry. Remote Sens. 9, 1110. https://doi.org/10.3390/rs9111110

Amatulli, G., Domisch, S., Tuanmu, M.-N., Parmentier, B., Ranipeta, A., Malczyk, J., Jetz, W., 2018. A suite of global, cross-scale topographic variables for environmental and biodiversity modeling. Sci. Data 2018 51 5, 1–15. https://doi.org/10.1038/sdata.2018.40

Anders, N., Smith, M., Suomalainen, J., Cammeraat, E., Valente, J., Keesstra, S., 2020. Impact of flight altitude and cover orientation on Digital Surface Model (DSM) accuracy for flood damage assessment in Murcia (Spain) using a fixed-wing UAV. Earth Sci. Informatics 13, 391–404. https://doi.org/10.1007/s12145-019-00427-7

Balta, H., De Cubber, G., Baudoin, Y., Doroftei, D., Balta, H., Doroftei, D., Baudoin, Y., De Cubber, G., Baudoin, Y., Doroftei, D., Balta, H., Doroftei, D., Baudoin, Y., 2015. UAS deployment and data processing during the Balkans flooding with the support to Mine Action, in: 8th IARP Workshop on Robotics for Risky Environments. Institute of Electrical and Electronics Engineers Inc. https://doi.org/10.1109/SSRR.2014.7017670

Barnes, C.F., Fritz, H., Yoo, J., 2007. Hurricane disaster assessments with image-driven data mining in high-resolution satellite imagery. IEEE Trans. Geosci. Remote Sens. 45, 1631–1640. https://doi.org/10.1109/TGRS.2007.890808

Bell, J.R., Gebremichael, E., Molthan, A., Schultz, L., Meyer, F., Shrestha, S., 2019. Synthetic Aperture Radar and Optical Remote Sensing of Crop Damage Attributed to Severe Weather in the Central United States, in: International Geoscience and Remote Sensing Symposium (IGARSS). Institute of Electrical and Electronics Engineers Inc., pp. 9938–9941. https://doi.org/10.1109/IGARSS.2019.8899775

Bertin, S., Levy, B., Gee, T., Delmas, P., 2020. Geomorphic Change Detection Using Cost-Effective Structure-from-Motion Photogrammetry: Evaluation of Direct Georeferencing from Consumer-Grade UAS at Orewa Beach (New Zealand). Photogramm. Eng. Remote Sens. 86, 289–298. https://doi.org/10.14358/PERS.86.5.289

Bodoque, J., Guardiola-Albert, C., Aroca-Jiménez, E., Eguibar, M., Martínez-Chenoll, M., 2016. Flood Damage Analysis: First Floor Elevation Uncertainty Resulting from LiDAR-Derived

Digital Surface Models. Remote Sens. 8, 604. https://doi.org/10.3390/rs8070604

Brodie, K., Spore, N., Bruder, B., Renaud, A., Hesser, T., Wilhelm, V., Hodgens, K., 2019. Post-Irma Unmanned Aircraft System (UAS) Coastal Storm Impact Surveys. https://doi.org/10.21079/11681/32463

Carvajal-Ramírez, F., Marques da Silva, J.R., Agüera-Vega, F., Martínez-Carricondo, P., Serrano, J., Moral, F.J., 2019. Evaluation of Fire Severity Indices Based on Pre- and Post-Fire Multispectral Imagery Sensed from UAV. Remote Sens. 11, 993. https://doi.org/10.3390/rs11090993

Castro, C.C., Gómez, J.A.D., Martín, J.D., Sánchez, B.A.H., Arango, J.L.C., Tuya, F.A.C., Díaz-Varela, R., 2020. An UAV and satellite multispectral data approach to monitor water quality in small reservoirs. Remote Sens. 12, 1514. https://doi.org/10.3390/RS12091514

Chen, Z., Wagner, M., Das, J., Doe, R.K., Cerveny, R.S., 2021. Data-Driven Approaches for Tornado Damage Estimation with Unpiloted Data-Driven Approaches for Tornado Damage Estimation with Unpiloted Aerial Systems. https://doi.org/10.3390/rs13091669

Choi, K., Lee, I., 2012. A UAV Based Close-Range Rapid Aerial Monitoring System for Emergency Responses. Int. Arch. Photogramm. Remote Sens. Spat. Inf. Sci. XXXVIII-1/, 247–252. https://doi.org/10.5194/isprsarchives-xxxviii-1-c22-247-2011

Choi, K., Lee, I., Hong, J., Oh, T., Shin, S.W., 2009. Developing a UAV-based rapid mapping system for emergency response, in: Gerhart, G.R., Gage, D.W., Shoemaker, C.M. (Eds.), Unmanned Systems Technology XI. SPIE, p. 733209. https://doi.org/10.1117/12.818492

Choi, Y., Pate, D., Briceno, S., Mavris, D.N., 2019. Rapid and Automated Urban Modeling Techniques for UAS Applications, in: 2019 International Conference on Unmanned Aircraft Systems, ICUAS 2019. Institute of Electrical and Electronics Engineers Inc., pp. 838–847. https://doi.org/10.1109/ICUAS.2019.8797943

Cooner, A.J., Shao, Y., Campbell, J.B., 2016. Detection of Urban Damage Using Remote Sensing and Machine Learning Algorithms: Revisiting the 2010 Haiti Earthquake. Remote Sens. 8. https://doi.org/10.3390/rs8100868

D'Oleire-Oltmanns, S., Marzolff, I., Peter, K.D., Ries, J.B., 2012. Unmanned Aerial Vehicle (UAV) for Monitoring Soil Erosion in Morocco. Remote Sens. 4, 3390–3416. https://doi.org/10.3390/rs4113390

De Reu, J., Bourgeois, J., De Smedt, P., Zwertvaegher, A., Antrop, M., Bats, M., De Maeyer, P.,

Finke, P., Van Meirvenne, M., Verniers, J., Crombé, P., 2011. Measuring the relative topographic position of archaeological sites in the landscape, a case study on the Bronze Age barrows in northwest Belgium. J. Archaeol. Sci. 38, 3435–3446. https://doi.org/10.1016/j.jas.2011.08.005

de Roos, S., Turner, D., Lucieer, A., Bowman, D.M.J.S., 2018. Using Digital Surface Models from UAS Imagery of Fire Damaged Sphagnum Peatlands for Monitoring and Hydrological Restoration. Drones 2, 45. https://doi.org/10.3390/drones2040045

Dominici, D., Alicandro, M., Massimi, V., 2017. UAV photogrammetry in the post-earthquake scenario: case studies in L'Aquila. Geomatics, Nat. Hazards Risk 8, 87–103. https://doi.org/10.1080/19475705.2016.1176605

Esri, 2021. arcgis.learn module — arcgis 1.9 documentation [WWW Document]. URL https://developers.arcgis.com/python/api-reference/arcgis.learn.toc.html# (accessed 8.28.21).

Fujita, A., Sakurada, K., Imaizumi, T., Ito, R., Hikosaka, S., Nakamura, R., 2017. Damage Detection from Aerial Images via Convolutional Neural Networks. Proc. 15th IAPR Int. Conf. Mach. Vis. Appl. MVA 2017 5–8. https://doi.org/10.23919/MVA.2017.7986759

Ghaffarian, S., Kerle, N., 2019. Towards Post-disaster Debris Identification for Precise Damage and Recovery Assessments from UAV and Satellite Images. ISPRS - Int. Arch. Photogramm. Remote Sens. Spat. Inf. Sci. XLII-2/W13, 297–302. https://doi.org/10.5194/isprs-archives-XLII-2-W13-297-2019

Ghassemian, H., 2016. A review of remote sensing image fusion methods. Inf. Fusion. https://doi.org/10.1016/j.inffus.2016.03.003

Gupta, R.P., 2017. Remote sensing geology: Third edition, Remote Sensing Geology: Third Edition. https://doi.org/10.1007/978-3-662-55876-8

Haala, N., Cramer, M., Rothermel, M., 2013. Quality of 3D Point Clouds from Highly Overlapping UAV Imagery. Int. Arch. Photogramm. Remote Sens. Spat. Inf. Sci. XL-1/W2, 183–188. https://doi.org/10.5194/isprsarchives-xl-1-w2-183-2013

Hallermann, N., Morgenthal, G., Rodehorst, V., 2015. Unmanned Aerial Systems (UAS) – Case Studies of Vision Based Monitoring of Ageing Structures, in: International Symposium Non-Destructive Testing in Civil Engineering (NDT-CE).

Heydari, S.S., Mountrakis, G., 2019. Meta-analysis of deep neural networks in remote sensing: A

comparative study of mono-temporal classification to support vector machines. ISPRS J. Photogramm. Remote Sens. 152, 192–210. https://doi.org/10.1016/j.isprsjprs.2019.04.016

Honkavaara, E., Litkey, P., Nurminen, K., 2013. Automatic Storm Damage Detection in Forests Using High-Altitude Photogrammetric Imagery. Remote Sens. 5, 1405–1424. https://doi.org/10.3390/rs5031405

Huang, B., Zhao, B., Song, Y., 2018. Urban land-use mapping using a deep convolutional neural network with high spatial resolution multispectral remote sensing imagery. Remote Sens. Environ. 214, 73–86. https://doi.org/10.1016/j.rse.2018.04.050

Isibue, E.W., Pingel, T.J., 2020. Unmanned aerial vehicle based measurement of urban forests. Urban For. Urban Green. 48, 126574. https://doi.org/10.1016/j.ufug.2019.126574

Jasiewicz, J., Stepinski, T.F., 2013. Geomorphons-a pattern recognition approach to classification and mapping of landforms. Geomorphology 182, 147–156. https://doi.org/10.1016/j.geomorph.2012.11.005

Ji, S., Zhang, C., Xu, A., Shi, Y., Duan, Y., 2018. 3D Convolutional Neural Networks for Crop Classification with Multi-Temporal Remote Sensing Images. Remote Sens. 10, 75. https://doi.org/10.3390/rs10010075

Karimi, A., Madadi, M., Abdollahi, S., Ostad-Ali-Askari, K., Eslamian, S., P. Singh, V., 2019. Determination of Fire Extent in Forest Zones Using Remote Sensing Data Case Study: Golestan Province of Iran. J. Geogr. Cartogr. 2. https://doi.org/10.24294/jgc.v2i1.753

Kemker, R., Salvaggio, C., Kanan, C., 2018. Algorithms for semantic segmentation of multispectral remote sensing imagery using deep learning. ISPRS J. Photogramm. Remote Sens. 145, 60–77. https://doi.org/10.1016/j.isprsjprs.2018.04.014

Kingfield, D.M., de Beurs, K.M., 2017. Landsat Identification of Tornado Damage by Land Cover and an Evaluation of Damage Recovery in Forests. J. Appl. Meteorol. Climatol. 56, 965–987. https://doi.org/10.1175/JAMC-D-16-0228.1

Kong, H., Akakin, H.C., Sarma, S.E., 2013. A Generalized Laplacian of Gaussian Filter for Blob Detection and Its Applications. IEEE Trans. Cybern. 43, 1719–1733. https://doi.org/10.1109/TSMCB.2012.2228639

Lin, A.Y.M., Novo, A., Har-Noy, S., Ricklin, N.D., Stamatiou, K., 2011. Combining GeoEye-1 Satellite Remote Sensing, UAV Aerial Imaging, and Geophysical Surveys in Anomaly Detection Applied to Archaeology. IEEE J. Sel. Top. Appl. Earth Obs. Remote Sens. 4,

870–876. https://doi.org/10.1109/JSTARS.2011.2143696

Ma, H., Liu, Y., Ren, Y., Wang, D., Yu, L., Yu, J., 2020. Improved CNN Classification Method for Groups of Buildings Damaged by Earthquake, Based on High Resolution Remote Sensing Images. Remote Sens. 12, 260. https://doi.org/10.3390/rs12020260

Mahdianpari, M., Salehi, B., Rezaee, M., Mohammadimanesh, F., Zhang, Y., 2018. Very Deep Convolutional Neural Networks for Complex Land Cover Mapping Using Multispectral Remote Sensing Imagery. Remote Sens. 10, 1119. https://doi.org/10.3390/rs10071119

Menderes, A., Erener, A., Sarp, G., 2015. Automatic Detection of Damaged Buildings after Earthquake Hazard by Using Remote Sensing and Information Technologies. Procedia Earth Planet. Sci. 15, 257–262. https://doi.org/10.1016/j.proeps.2015.08.063

Mohammadi, M.E., Watson, D.P., Wood, R.L., 2019. Deep learning-based damage detection from aerial SFM point clouds. Drones 3, 1–29. https://doi.org/10.3390/drones3030068

Mulero-Pázmány, M., Barasona, J.Á., Acevedo, P., Vicente, J., Negro, J.J., 2015. Unmanned Aircraft Systems complement biologging in spatial ecology studies. Ecol. Evol. 5, 4808–4818. https://doi.org/10.1002/ece3.1744

Murphy, R., Dufek, J., Sarmiento, T., Wilde, G., Xiao, X., Braun, J., Mullen, L., Smith, R., Allred, S., Adams, J., Wright, A., Gingrich, J., 2016. Two case studies and gaps analysis of flood assessment for emergency management with small unmanned aerial systems, in: SSRR 2016 - International Symposium on Safety, Security and Rescue Robotics. Institute of Electrical and Electronics Engineers Inc., pp. 54–61. https://doi.org/10.1109/SSRR.2016.7784277

Nagarajan, S., Khamaru, S., De Witt, P., 2019. UAS based 3D shoreline change detection of Jupiter Inlet Lighthouse ONA after Hurricane Irma. Int. J. Remote Sens. 40, 9140–9158. https://doi.org/10.1080/01431161.2019.1569792

NWS, 2019. Tornadoes of April 19th, 2019 [WWW Document]. URL https://www.weather.gov/rnk/2019_04_19_Tornado (accessed 10.19.20).

NWS, 2018. Post-Storm Data Acquisition [WWW Document]. URL http://www.nws.noaa.gov/directives/sym/pd08003003curr.pdf

Ogden, L.E., 2013. Drone Ecology. Bioscience. https://doi.org/10.1525/bio.2013.63.9.18

Palsson, F., Sveinsson, J.R., Ulfarsson, M.O., Benediktsson, J.A., 2015. Model-based fusion of multi-and hyperspectral images using PCA and wavelets. IEEE Trans. Geosci. Remote

Sens. 53, 2652–2663. https://doi.org/10.1109/TGRS.2014.2363477

Papakonstantinou, A., Doukari, M., Moustakas, A., Chrisovalantis, D., Chaidas, K., Roussou, O., Athanasis, N., Topouzelis, K., Soulakellis, N., 2018. UAS multi-camera rig for post-earthquake damage 3D geovisualization of Vrisa village, in: Themistocleous, K., Hadjimitsis, D.G., Michaelides, S., Ambrosia, V., Papadavid, G. (Eds.), Sixth International Conference on Remote Sensing and Geoinformation of the Environment (RSCy2018). SPIE, p. 52. https://doi.org/10.1117/12.2326173

Pedregosa, F., Varoquaux, G., Gramfort, A., Michel, V., Thirion, B., Grisel, O., Blondel, M., Prettenhofer, P., Weiss, R., Dubourg, V., Vanderplas, J., Passos, A., Cournapeau, D., Brucher, M., Perrot, M., Duchesnay, E., 2011. Scikit-learn: Machine Learning in Python. J. Mach. Learn. Res. 12, 2825–2830.

Peng, C., Xu, Z., Yang, J., Zheng, Y., Wang, W., Liu, S., Tian, B., 2018. Development of an UAS for Earthquake Emergency Response and Its Application in Two Disastrous Earthquakes, in: Earthquakes - Forecast, Prognosis and Earthquake Resistant Construction. InTech. https://doi.org/10.5772/intechopen.76885

Pingel, T.J., Saavedra, A., Cobo, L., 2001. Deriving Land and Water Surface Elevations in the Northeastern Yucatán Peninsula using PPK GPS and UAV-based Structure from Motion. Appl. Geogr.

Prabhakar, M., Gopinath, K.A., Reddy, A.G.K., Thirupathi, M., Rao, C.S., 2019. Mapping hailstorm damaged crop area using multispectral satellite data. Egypt. J. Remote Sens. Sp. Sci. 22, 73–79. https://doi.org/10.1016/j.ejrs.2018.09.001

Psomiadis, E., Soulis, K.X., Zoka, M., Dercas, N., 2019. Synergistic Approach of Remote Sensing and GIS Techniques for Flash-Flood Monitoring and Damage Assessment in Thessaly Plain Area, Greece. Water (Switzerland) 11, 448. https://doi.org/10.3390/w11030448

Radhika, S., Tamura, Y., Matsui, M., 2015. Cyclone damage detection on building structures from pre- and post-satellite images using wavelet based pattern recognition. J. Wind Eng. Ind. Aerodyn. 136, 23–33. https://doi.org/10.1016/j.jweia.2014.10.018

Rahman, M.S., Di, L., 2017. The state of the art of spaceborne remote sensing in flood management. Nat. Hazards. https://doi.org/10.1007/s11069-016-2601-9

Riley, S., 1999. Index that quantifies topographic heterogeneity. Intermt. J. Sci.

Rogers, S.R., Manning, I., Livingstone, W., 2020. Comparing the Spatial Accuracy of Digital Surface Models from Four Unoccupied Aerial Systems: Photogrammetry Versus LiDAR. Remote Sens. 12, 2806. https://doi.org/10.3390/rs12172806

Salmoral, G., Casado, M.R., Muthusamy, M., Butler, D., Menon, P.P., Leinster, P., 2020. Guidelines for the use of unmanned aerial systems in flood emergency response. Water (Switzerland). https://doi.org/10.3390/w12020521

Salvo, G., Caruso, L., Scordo, A., 2014. Urban Traffic Analysis through an UAV. Procedia - Soc. Behav. Sci. 111, 1083–1091. https://doi.org/10.1016/j.sbspro.2014.01.143

Samiappan, S., Hathcock, L., Turnage, G., McCraine, C., Pitchford, J., Moorhead, R., 2019. Remote Sensing of Wildfire Using a Small Unmanned Aerial System: Post-Fire Mapping, Vegetation Recovery and Damage Analysis in Grand Bay, Mississippi/Alabama, USA. Drones 3, 1–18. https://doi.org/10.3390/drones3020043

Sappington, J.M., Longshore, K.M., Thompson, D.B., 2007. Quantifying Landscape Ruggedness for Animal Habitat Analysis: A Case Study Using Bighorn Sheep in the Mojave Desert. J. Wildl. Manage. 71, 1419–1426. https://doi.org/10.2193/2005-723

Schmidt, J., Evans, I.S., Brinkmann, J., 2003. Comparison of polynomial models for land surface curvature calculation. Int. J. Geogr. Inf. Sci. 17, 797–814. https://doi.org/10.1080/13658810310001596058

Seier, G., Kellerer-Pirklbauer, A., Wecht, M., Hirschmann, S., Kaufmann, V., Lieb, G.K., Sulzer, W., 2017. UAS-Based Change Detection of the Glacial and Proglacial Transition Zone at Pasterze Glacier, Austria. Remote Sens. 9, 549. https://doi.org/10.3390/rs9060549

Shen, H., Huang, L., Zhang, L., Wu, P., Zeng, C., 2016. Long-term and fine-scale satellite monitoring of the urban heat island effect by the fusion of multi-temporal and multi-sensor remote sensed data: A 26-year case study of the city of Wuhan in China. Remote Sens. Environ. 172, 109–125. https://doi.org/10.1016/j.rse.2015.11.005

Singh, S.K., Kanga, S., 2017. Forest Fire Simulation Modeling using Remote Sensing & GIS. Int. J. Adv. Res. Comput. Sci. 8, 326–332.

Skow, K.D., Cogil, C., 2017. A high-resolution aerial survey and radar analysis of quasi-linear convective system surface vortex damage paths from 31 August 2014. Weather Forecast. 32, 441–467. https://doi.org/10.1175/WAF-D-16-0136.1

Thomas, J., Kareem, A., Bowyer, K., 2013. Recent advances towards a robust, automated

hurricane damage assessment from high resolution images, in: Advances in Hurricane Engineering: Learning from Our Past - Proceedings of the 2012 ATC and SEI Conference on Advances in Hurricane Engineering. pp. 806–815. https://doi.org/10.1061/9780784412626.069

Tian, J., Nielsen, A.A., Reinartz, P., 2015. Building damage assessment after the earthquake in Haiti using two post-event satellite stereo imagery and DSMs. Int. J. Image Data Fusion 6, 155–169. https://doi.org/10.1080/19479832.2014.1001879

Tuia, D., Marcos, D., Camps-Valls, G., 2016. Multi-temporal and multi-source remote sensing image classification by nonlinear relative normalization. ISPRS J. Photogramm. Remote Sens. 120, 1–12. https://doi.org/10.1016/j.isprsjprs.2016.07.004

Udo, K., Takeda, Y., Koshimura, S., 2018. Detection of Coastal Damage using Differences in Automatically Generated Digital Surface Models (DSMs): Application to the 2011 off the Pacific Coast of Tohoku Earthquake Tsunami, in: Journal of Coastal Research. Coastal Education Research Foundation Inc., pp. 696–700. https://doi.org/10.2112/SI85-140.1

Van Iersel, W.K., Straatsma, M.W., Addink, E.A., Middelkoop, H., 2016. Monitoring phenology of floodplain grassland and herbaceous vegetation with UAV imagery, in: International Archives of the Photogrammetry, Remote Sensing and Spatial Information Sciences - ISPRS Archives. pp. 569–571. https://doi.org/10.5194/isprsarchives-XLI-B7-569-2016

Vetrivel, A., Kerle, N., Gerke, M., Nex, F., Vosselman, G., 2016. Towards automated satellite image segmentation and classification for assessing disaster damage using data-specific features with incremental learning. University Library/University of Twente. https://doi.org/10.3990/2.369

Wagner, M., Chen, Z., Das, J., Doe, R.K., Cerveny, R.S., 2020. Detecting and Classifying Tornado Damage Utilizing Deep Neural Networks and UAS-Based Imagery, in: 100th American Meteorological Society Annual Meeting.

Wagner, M., Doe, R.K., Johnson, A., Chen, Z., Das, J., Cerveny, R.S., 2019. Unpiloted Aerial Systems (UASs) Application for Tornado Damage Surveys: Benefits and Procedures. Bull. Am. Meteorol. Soc. 100, 2405–2409. https://doi.org/10.1175/BAMS-D-19-0124.1

Waite, C.E., van der Heijden, G.M.F., Field, R., Boyd, D.S., 2019. A view from above: Unmanned aerial vehicles (UAVs) provide a new tool for assessing liana infestation in tropical forest canopies. J. Appl. Ecol. 56, 902–912. https://doi.org/10.1111/1365-

2664.13318

Westoby, M.J., Brasington, J., Glasser, N.F., Hambrey, M.J., Reynolds, J.M., 2012. 'Structure-from-Motion' photogrammetry: A low-cost, effective tool for geoscience applications. Geomorphology 179, 300–314. https://doi.org/10.1016/J.GEOMORPH.2012.08.021

Womble, J.A., Wood, R.L., Mohammadi, M.E., 2018. Multi-scale remote sensing of tornado effects. Front. Built Environ. 4. https://doi.org/10.3389/fbuil.2018.00066

Wood, J., 1996. The geomorphological characterisation of Digital Elevation Models.

Xu, X., Quan, C., Ren, F., 2015. Facial expression recognition based on Gabor Wavelet transform and Histogram of Oriented Gradients, in: 2015 IEEE International Conference on Mechatronics and Automation, ICMA 2015. Institute of Electrical and Electronics Engineers Inc., pp. 2117–2122. https://doi.org/10.1109/ICMA.2015.7237813

Xu, Z., Wu, L., Zhang, Z., Wu, L., 2018. Use of active learning for earthquake damage mapping from UAV photogrammetric point clouds. Int. J. Remote Sens. 39, 5568–5595. https://doi.org/10.1080/01431161.2018.1466083

Yamazaki, F., Liu, W., 2016. Remote Sensing Technologies for Post-Earthquake Damage Assessment: A Case Study on the 2016 Kumamoto Earthquake, ASIA Conference on Earthquake Engineering.

Yamazaki, F., Matsuda, T., Denda, S., Liu, W., 2015. Construction of 3D models of buildings damaged by earthquakes using UAV aerial images. Proc. Tenth Pacific Conf. Earthq. Eng. Build. an Earthquake-Resilient Pacific.

Yokoyama, R., Shirasawa, M., Pike, R.J., 2002. Visualizing topography by openness: A new application of image processing to digital elevation models. Photogramm. Eng. Remote Sensing 68, 257–265.

Yuan, M., Dickens-Micozzi, M., Magsig, M.A., 2002. Analysis of tornado damage tracks from the 3 May tornado outbreak using multispectral satellite imagery. Weather Forecast. 17, 382–398. https://doi.org/10.1175/1520-0434(2002)017<0382:AOTDTF>2.0.CO;2

Zhou, J., Pavek, M.J., Shelton, S.C., Holden, Z.J., Sankaran, S., 2016. Aerial multispectral imaging for crop hail damage assessment in potato. Comput. Electron. Agric. 127, 406–412. https://doi.org/10.1016/j.compag.2016.06.019